
Terahertz Lasers Based on Intersubband Transitions

Personnel

B. Williams, H. Callebaut, S. Kumar, and Q. Hu, in collaboration with J. Reno

Sponsorship

NSF, ARO, AFOSR, and NASA

Semiconductor quantum wells are human-made quantum mechanical systems in which the energy levels can be designed and engineered to be of any value. Consequently, unipolar lasers based on intersubband transitions (electrons that make lasing transitions between subband levels within the conduction band) were proposed for long-wavelength sources as early as the 1970s. However, because of the great challenge in epitaxial material growth and the unfavorable fast non-radiative relaxation rate, unipolar intersubband-transition lasers (also called quantum-cascade lasers) at mid-infrared wavelengths were developed only recently at Bell Laboratories. This achievement is remarkable, but the technique used in the original quantum-cascade lasers will not be directly applicable for the longer-wavelength THz range because of two major obstacles. First, the energy levels corresponding to THz frequencies ($1 \text{ THz} = 4 \text{ meV}$) are quite narrow, so the requirements for the design and fabrication of suitable quantum wells are demanding. Because of the narrow separation between subband levels, heating and electron-electron scattering will have a much greater effect. Also, the small energy scales of THz photons make the detection and analysis of spontaneous emission (a crucial step toward developing lasers) quite difficult. Second, mode confinement, which is essential for any laser oscillation, is difficult at longer wavelengths.

Conventional dielectric-waveguide confinement is not applicable because the evanescent field penetration, which is proportional to the wavelength and is on the order of several tens of microns, is much greater than the active gain medium of several microns. Currently, we are investigating to overcome these two obstacles in order to develop intersubband-transition lasers. We have made good success in generating and detecting THz emission signals and on developing a novel mode confinement method using metallic waveguide structures. Key results are summarized in the following sections.

THz emitters using electron-LO-phonon scattering for depopulation

Following the design principle of the original QCLs, we have designed intersubband THz emitters based on a three-level system. The top two subband levels, E_3 and E_2 , form the radiative pair, while the ground state E_1 is at below E_2 . Since it is energetically allowed, the fast electron-LO-phonon $E_2 \rightarrow E_1$ scattering will help to keep the population in E_2 low, and therefore maintain a population inversion between E_3 and E_2 . However, because $E_3 - E_2 < E_2 - E_1$ for THz emitters, it is difficult to implement this three-level system based on an intrawell transition scheme, in which both E_3 and E_2 are primarily located in a single well. The bottom of this well would have to be raised relative to the rest of the structure so that $E_2 - E_1 \geq \hbar\omega_{LO}$. Raising the bottom of the well would require adding aluminum to the well material GaAs, which would cause a significant alloying scattering and result in a broad emission linewidth.

Our design of the three-level systems is based on a scheme that the radiative transition takes place in a coupled double-well structure. A third well, which is much wider than the two wells, contains the ground-state level E_1 . In our earlier designs, the wave functions of E_3 and E_2 are primarily localized in separate wells, thus the $E_3 \rightarrow E_2$ transition is spatially diagonal. This design offers the advantage of a high selectivity in injection into E_3 and removal from E_2 , because of the spatial separation of the two wave functions. However, the diagonal nature of the radiative transition is quite sensitive to scattering due to interface roughness and alloy in the barrier, and thus the emission showed rather broad spectra ($\Delta f \sim 3\text{-}5 \text{ THz}$).

It is well known that in a coupled double-well structure, the wave functions of the two lowest levels are spatially extended with a strong overlap at the anti-crossing. Because of this spatial overlap, both levels are subject to the same interface and alloy scattering, and

thus the emission linewidth of radiative transition between the two levels is reduced. In an improved structure, whose band structure and wave functions are shown in Figure 1, we have taken advantage of this feature to enhance the strength of the radiative $E_3 \rightarrow E_2$ transition. In the structure shown in Fig. 1, the core is a three-well module of GaAs/Al_{0.3}Ga_{0.7}As heterostructures (inside the dashed box), with three barriers B₁ (4.5 nm), B₂ (2.8 nm), B₃ (5.6 nm) and three wells W₁ (8.8 nm), W₂ (5.9 nm), and W₃ (6.8 nm). The collector barrier B₁ is center δ -doped at a level of $6 \times 10^{10}/\text{cm}^2$ in order to provide dynamic charges. Under the designed bias of 51 mV per module, the ground state E_1' (not shown) of a previous module is aligned with E_3 . Thus, the upper level E_3 can be selectively populated via resonant tunneling. At this bias, the energy separation $E_{32} \approx 11$ meV (corresponding to 2.67 THz), and the dipole moment $z_{32} \approx 30$ Å. The energy separation $E_{21} \approx 40$ meV $\geq \hbar\omega_{LO}$, enabling electron-LO-phonon $E_2 \rightarrow E_1$ scattering for depopulation.

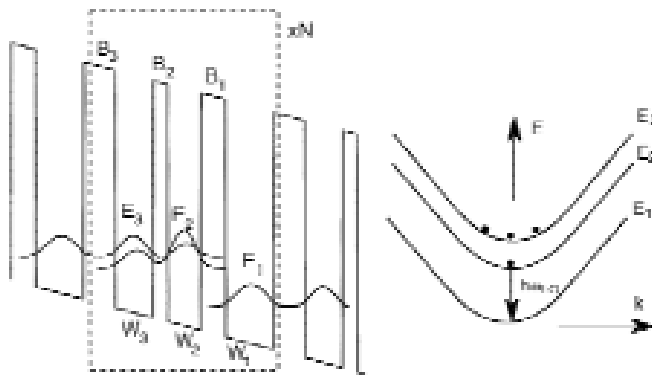


Fig. 40: Schematic of a three-level system based on a triple quantum-well structure shown inside the dashed box. On the right is the dispersion relation between the energy and the transverse momentum.

In order to measure the intersubband THz emission and resolve its spectra, we constructed a set-up that included a Fourier Transform Infrared Spectrometer

(FTIR) with a composite Si bolometer as its detector. The system's schematic is shown in Figure 41. We have improved this system and perfected our measurement techniques so that THz emission measurements can be routinely performed on our emitters with output power levels of 1-10 pW.

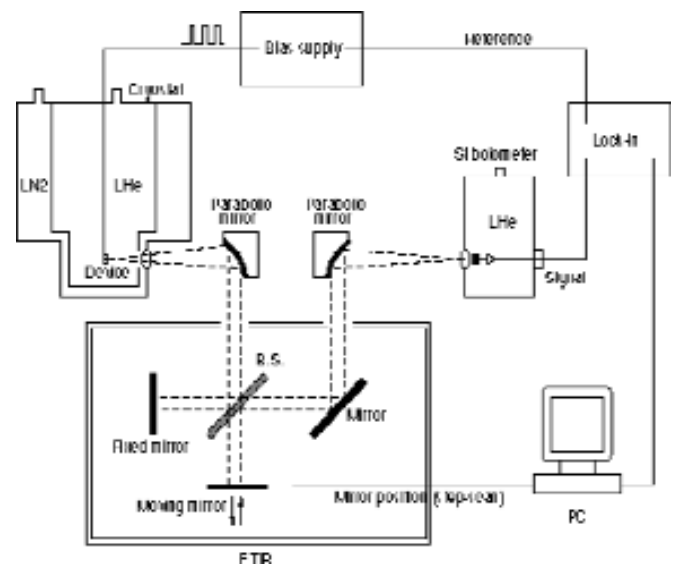


Fig. 41: Far-infrared measurement set-up that uses a Fourier transform spectrometer to spectrally resolve the emitted THz signals.

Our emission spectra reveal a clear peak due to the $E_3 \rightarrow E_2$ intersubband emission. A representative spectrum taken at 5-K device temperature is shown in Fig. 3(a), which was taken at the designed bias of 1.6 V ($\sim 30 \times 51$ mV). The measured peak frequency of 2.57 THz (10.6 meV) is close to the designed value of 11.3 meV. The FWHM linewidth is as narrow as 0.47 THz (1.9 meV). In order to verify the intersubband origin of the measured emission spectra, we have measured emission spectrum at a high bias of 4.0 V at which the energy levels are severely misaligned. The spectrum is shown in the inset of Figure 42(a), and it bears little resemblance to the main figure.

Spectra were also taken with the cold stage cooled with liquid nitrogen to 80 K. One taken at a bias of 1.6 V is shown in Figure 42(b). The main peak is essentially the same as the one measured at 5 K, with a slightly broader linewidth of 0.52 THz (2.14 meV). The linewidth measured at 80 K is expected to be similar to that at 5 K, since nonparabolicity is negligible for THz intersubband emitters. Nevertheless, our experimental verification is encouraging for the development of intersubband THz sources at elevated temperatures.

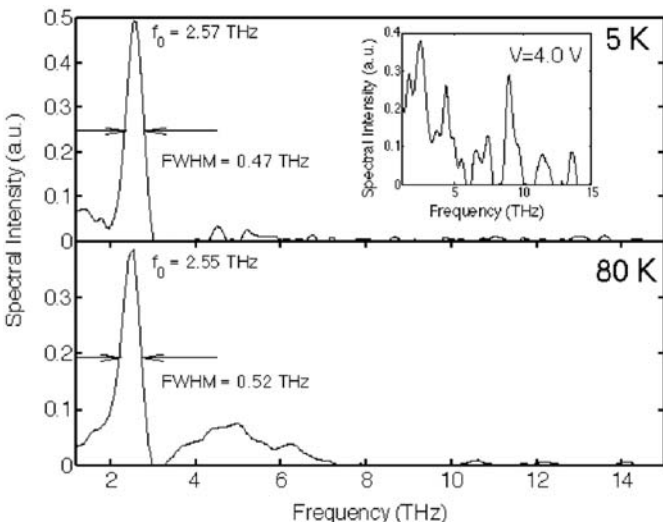


Fig. 42: Spectrally resolved THz intersubband spontaneous emission taken at (a) 5-K and (b) 80-K bath temperature under 1.6-V bias. The inset shows the spectrum for 4.0-V bias, clear evidence that emission results from intersubband transitions.

Role of interface and confined phonon modes

Just like the electronic wave functions forming discrete subbands in MQW structures, phonon spectra also become discrete, forming spatially localized interface and confined modes. Despite this parallel analogy, bulk LO-phonon mode has been used to calculate the scattering times in QCLs. This practice may be justified for mid-infrared QC lasers, in which $E_3 - E_2 \gg \hbar\omega_{LO}$, so that the sum-rule yields the same result as obtained from using

the bulk mode. However, as Dutta and Stroschio recently pointed out, such a practice may be questionable for THz intersubband lasers, because $E_3 - E_2 < \hbar\omega_{LO}$ and $E_2 - E_1 \approx \hbar\omega_{LO}$.

We have investigated the role of the complex phonon spectra on the intersubband scattering rates. In the model used in our calculations, the phonon modes are described by the potential $\phi(\mathbf{r})$ resulting from the polarization field created by atomic displacements in a polar semiconductor. Each material layer of index i is described by a dielectric function $\epsilon_i(\omega)$ as given by the Lyddane-Sachs-Teller relations, which vanishes at the LO-phonon frequencies. For lattice vibrations, since there are no free charges, the phonon potential must satisfy $\epsilon(\omega) - \nabla^2\phi(\mathbf{r}) = 0$. Two types of solutions exist: interface modes for which $\nabla^2\phi(\mathbf{r})=0$, and confined modes for which $\epsilon(\omega)=0$.

For the confined modes, $\epsilon(\omega)=0$ and therefore $\omega = \omega_{LO}$, where ω_{LO} is the bulk LO-phonon frequency in the layer of interest. Since ω_{LO} changes at the heterointerfaces, the potential must vanish there, and $\phi(\mathbf{r})$ can be described in terms of sine wave modes in z . For the interface modes, $\epsilon(\omega) \neq 0$, and the modes have frequencies $\omega \neq \omega_{LO}$. The potential solution is a linear combination of exponential terms peaked at the interfaces, hence the name of "interface mode". For our GaAs/AlGaAs quantum-well structures, there are usually two "GaAs-like" and one "AlAs-like" modes associated with each GaAs/AlGaAs interface. Thus, for the six interfaces in our triple-well structures shown in Figure 40, there are a total 18 interface modes. The total scattering rate is the sum of the contributions from these 18 interface modes and all the confined modes (30 lowest modes were used in our calculations with the contributions from the higher modes negligible).

We used the transfer matrix approach to account for the electromagnetic boundary conditions and obtain the mode potentials and dispersion relations for the

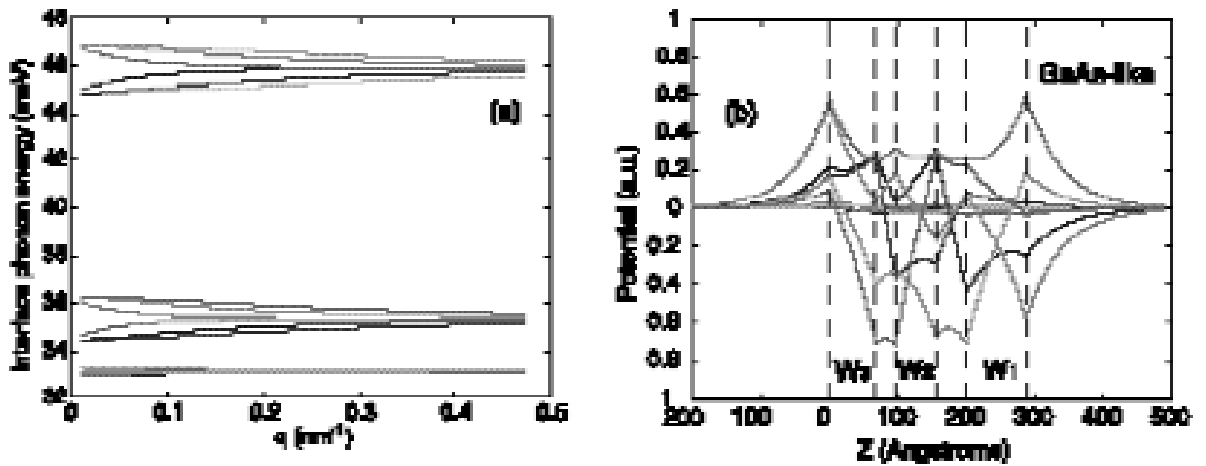


Fig. 43:(a) Dispersion relation of all the 18 interface modes; (b) phonon potential profiles of the 12 "GaAs-like" interface modes associated with our triple quantum-well device.

interface modes. As it turns out, the 12 "GaAs-like" modes are clustered around 33-36 meV, close to the bulk GaAs LO-phonon energy. The 6 "AlAs-like" modes are clustered around 45-47 meV, close to the bulk AlAs LO-phonon energy. Special care was taken to ensure a proper normalization of each mode, which was verified by limiting cases. The dispersion relation and the phonon potential profiles for the interface modes are shown in Figure 43.

In order to address the key issue of the optimum subband separation E_{21} , we have calculated the maximum total scattering rate as a function of E_{21} , as shown in Figure 44. The rate shows two peaks, one at ~ 35 meV due to the "GaAs-like" modes and the other at ~ 47 meV due to the "AlAs-like" modes. As a comparison, we also include the scattering rate calculated using the bulk GaAs LO-phonon mode. It is clear that the scattering rate is $\sim 30\%$ lower than the bulk mode if $E_{21} \sim 36$ meV, because of the exclusion of the "AlAs-like" modes. However, increasing E_{21} to ~ 47 meV does not increase the total scattering rate appreciably. This is because that at $E_{21} \sim 47$ meV, even though all the phonon modes participate in the scattering, the rapid

decrease in the strength of the "GaAs-like" modes away from their resonance (at ~ 36 meV) diminishes most of the benefit gained from including more active phonon modes.

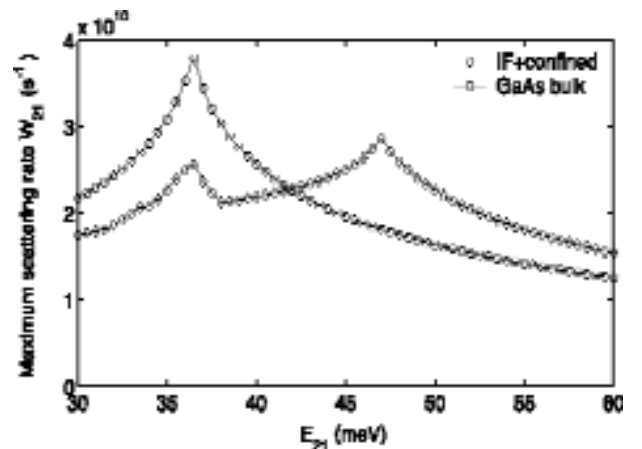


Fig. 44: Maximum scattering rate versus subband separation E_{21} for the three-level structure shown in Fig. 1. Maximum scattering rate calculated with GaAs bulk modes is present for comparison.

In Figure 45, we plot the key figure of merit $\tau_3(1 - \tau_{21}/\tau_{32})$, which is proportional to the population inversion Δn_{32} , as a function of the scattering time τ_{32} . As E_{21} increases from 36 to 47 meV, the increase in Δn_{32} is marginal at a given τ_{32} . Even this marginal increase should be taken with a grain of salt. As E_{21} increases from 36 to 47 meV, there will be an additional 11 meV energy dissipation per electron. This extra energy dissipation will further raise the electronic temperature. As a result, τ_{32} decreases because of LO-phonon scattering of hot electrons. Figure 45 shows that a reduction in τ_{32} could undo any advantage gained by increasing E_{21} to 47 meV. The conclusion from our analysis is that in electrically pumped THz intersubband emitters, because the barriers are thin and Al concentrations are low ($x \leq 0.3$), the contribution from the higher-energy "AlAs-like" modes only barely make up for the loss in the strength of "GaAs-like" modes. Thus, increasing E_{21} from 36 to 47 meV will only yield at the best a marginal (if any at all) improvement in population inversion Δn_{32} .

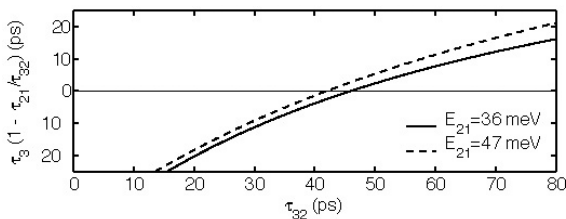


Fig. 45: Plot of the quantity $\tau_3(1 - \tau_{21}/\tau_{32})$, which is proportional to the population inversion Δn_{32} , versus the lifetime τ_{32} for the structure shown in Fig. 1.

Intrawell THz emitters using resonant tunneling for depopulation

Figure 46(a) shows the calculated band diagram of another type of THz intersubband emission structure that we investigated recently. In this structure, the radiative transition takes place between two subband levels primarily located in one quantum well. We consider this scheme as "intrawell" as opposed to the interwell scheme discussed earlier. It is known that the intrawell scheme

yields a larger dipole moment and a narrower emission linewidth, because the subband separation is less sensitive to impurity and interface roughness scattering.

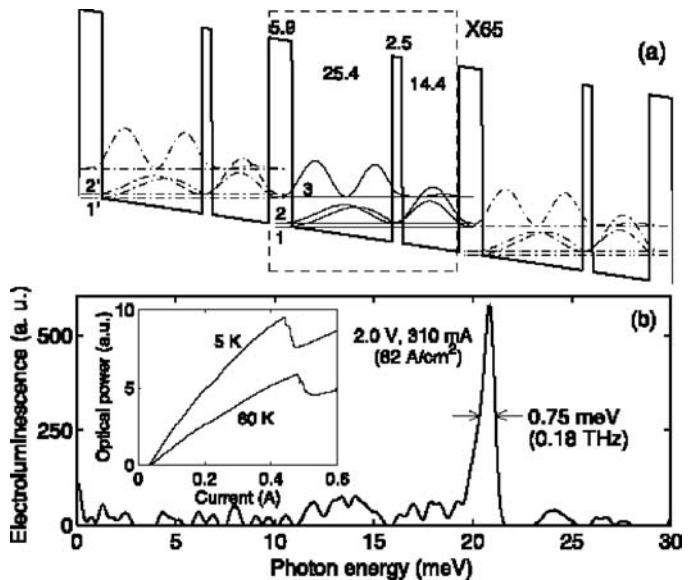


Fig. 46: (a) Computed conduction band profile and squared magnitude wave functions for the intrawell device. (b) Electroluminescence spectrum at 5 K for an applied bias of 2.0 V. The inset displays the emitted power versus current.

The core of the structure shown in Figure 46(a) is a coupled double-well module shown inside the dashed box. Sixty-five nominally identical modules are cascade connected. Under the designed bias of ~ 20 mV/module, the lower level E_2 in the wide well is aligned with the lowest level E_1 in the narrow well, which in turn is aligned with the upper level in the wide well of the following module. The radiative transition takes place between E_3 and E_2 , which have a strong spatial overlap as can be seen in Figure 46(a). The depopulation of E_2 is facilitated through "resonant tunneling" from E_2 to E_1 , which deserves special attention and will be discussed

in the following. The calculated dipole moment $z_{32} \approx 6.0$ nm at the designed bias, as a result of the strong radiative coupling in this intrawell scheme.

Figure 46(b) shows a measured emission spectrum taken at a bias of 2.0 V, which is somewhat greater than the designed bias (65×20 mV ≈ 1.3 V). The spectrum shows a clear peak at 21 meV (~ 5.04 THz), with a FWHM linewidth as narrow as 0.75 meV (0.18 THz). The measured emission frequency is close to the calculated subband separation $E_{32} \approx 18.5$ meV, and the narrow linewidth indicates the high quality of the MBE growth.

The term "resonant tunneling" usually refers to electron transport between two subband levels close in energies. There has been a long debate on whether this process should be analyzed as intersubband scattering between two spatially extended wave functions (the scenario of coherent resonant tunneling), or as tunneling between two spatially localized states (the scenario of incoherent sequential tunneling). This question is not merely academic, but is crucial for the successful development of intersubband THz lasers, as the two transport mechanisms yield very different depopulation rates. For coherent resonant tunneling, the electron transport is facilitated by fast (< 1 ps) electron-electron intersubband scattering. For incoherent sequential tunneling, the depopulation rate is determined by the barrier transparency, which can be much slower than the first scenario.

In the coherent picture, the energy difference between any pair of two subbands has a finite minimum value, known as the anti-crossing gap Δ , which characterizes how strongly the two subbands are coupled. In contrast, in the incoherent scenario, the two subband wave functions are spatially localized in different wells. Their energy levels can be degenerate and thus may be arbitrarily close at resonance. Based on the coherent model, we have calculated $\Delta_{21} = \min |E_2 - E_1| \approx 2.5$ meV. Even

though current-field (I - B) magneto-tunneling spectroscopy has been successfully used to resolved subband separations of ~ 20 meV, the resolution of the anti-crossing gaps of only a few meV requires the measurement of conductance $G = dI/dV$ to enhance the energy resolution and sensitivity.

Figure 47 shows both I - B and G - B curves measured in a voltage range near the E_2 - E_1 anti-crossing. The I - B curves show a single-period oscillation, revealing an energy separation of ~ 19 meV close to the calculated intersubband spacing. The G - B data show a closely separated double resonance, as highlighted by the double arrows. The dependence of these conductance peaks on bias is plotted in Figure 47(c), and it displays a typical anti-crossing behavior between a Stark shifted peak and another fixed at ~ 6.0 T (~ 21 meV). This 21-meV peak corresponds to $3 \rightarrow 2$ transition, which agrees with the emission data. The Stark shifted peak corresponds to $3 \rightarrow 1$ transition, as the two wave functions are spatially more separated than those of E_3 and E_2 . The minimum separation of the two conductance peaks is ~ 1.7 meV, which is close to the calculated anti-crossing gap of $\Delta_{21} \approx 2.5$ meV. The overall dependence of the conductance peaks on the bias agree reasonably well with the calculated energy differences E_{31} and E_{32} , as shown in Figure 47(c). Our work shows that in the particular structure shown in Figure 46(a), the $E_2 \rightarrow E_1$ depopulation should be modeled as intersubband scattering between two spatially extended states.

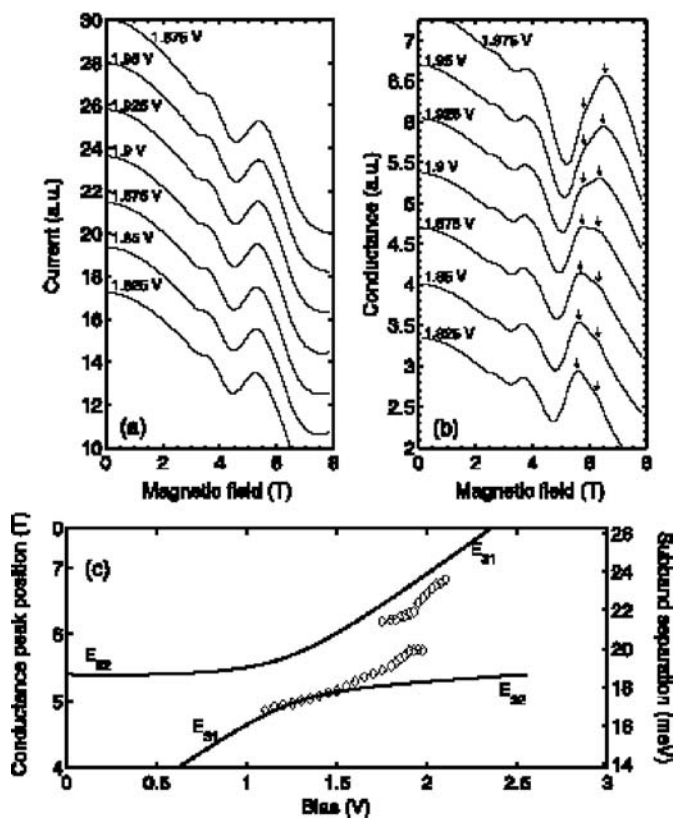


Fig. 47: Current (a) and conductance (b) versus magnetic field for several biases. (c) Positions of the double peaks in G-B plots versus the bias. The solid lines are calculated subband energy separation E_{32} and E_{31} .